Weierstraß-Institut
für Angewandte Analysis und Stochastik
Leibniz-Institut im Forschungsverbund Berlin e. V.

Preprint ISSN 2198-5855

Local control of globally competing patterns in coupled Swift–Hohenberg equations

Maximilian Becker[1], Thomas Frenzel[2], Thomas Niedermayer[1],

Sina Reichelt[2], Alexander Mielke[2,3], Markus Bär[1]

submitted: December 6, 2017

[1] Physikalisch-Technische Bundesanstalt
Abbestr. 2-12
10587 Berlin
Germany
E-Mail: maximilian.becker1@gmx.net
thomas.niedermayer@ptb.de
markus.baer@ptb.de

[2] Weierstrass Institute
Mohrenstr. 39
10117 Berlin
Germany
E-Mail: thomas.frenzel@wias-berlin.de firstname.lastname@wias-berlin.de
sina.reichelt@wias-berlin.de
alexander.mielke@wias-berlin.de

[3] Institut für Mathematik
Humboldt-Universität zu Berlin
Rudower Chaussee 25
12489 Berlin
Germany

No. 2457
Berlin 2017

Key words and phrases. Pattern formation, Swift–Hohenberg equation, weakly nonlinear analysis, amplitude equations, control.

M.B. and T.N. were supported by DFG within the SFB 910 via the project B5 “Control of multiscale reaction-diffusion patterns and application to biomembranes and cardiac dynamics” and S.R. was supported by DFG within the SFB 910 via the project A5 “Pattern formation in systems with multiple scales”. T.F. was supported by the European Research Council via the grant ERC-2010-AdG no. 267802 “Analysis of multiscale systems driven by functionals”.

Edited by
Weierstraß-Institut für Angewandte Analysis und Stochastik (WIAS)
Leibniz-Institut im Forschungsverbund Berlin e. V.
Mohrenstraße 39
10117 Berlin
Germany

Fax: +49 30 20372-303
E-Mail: preprint@wias-berlin.de
World Wide Web: http://www.wias-berlin.de/

Local control of globally competing patterns in coupled Swift–Hohenberg equations

Maximilian Becker, Thomas Frenzel, Thomas Niedermayer,
Sina Reichelt, Alexander Mielke, Markus Bär

Abstract

We present analytical and numerical investigations of two anti-symmetrically coupled 1D Swift–Hohenberg equations (SHEs) with cubic nonlinearities. The SHE provides a generic formulation for pattern formation at a characteristic length scale. A linear stability analysis of the homogeneous state reveals a wave instability in addition to the usual Turing instability of uncoupled SHEs. We performed weakly nonlinear analysis in the vicinity of the codimension-two point of the Turing-wave instability, resulting in a set of coupled amplitude equations for the Turing pattern as well as left and right traveling waves. In particular, these complex Ginzburg–Landau-type equations predict two major things: there exists a parameter regime where multiple different patterns are stable with respect to each other; and that the amplitudes of different patterns interact by local mutual suppression. In consequence, different patterns can coexist in distinct spatial regions, separated by localized interfaces. We identified specific mechanisms for controlling the position of these interfaces, which distinguish what kinds of patterns the interface connects and thus allow for global pattern selection. Extensive simulations of the original SHEs confirm our results.

Originally set up to describe convection instabilities, the Swift–Hohenberg equation (SHE) generically captures the formation of stationary patterns in nonequilibrium systems. A scalar parameter in this equation controls the bifurcation of a spatially homogeneous steady state to a so-called Turing-pattern, a stable stationary pattern with a finite length scale. In this paper, we consider two antisymmetrically coupled SHEs in one dimension. For comparable intrinsic length scales, the coupling gives rise to wave solutions emerging from an additional linear instability. A linear stability analysis of the homogeneous state allowed us to identify the codimension-two point where both patterns become unstable. Moreover, we have performed a weakly nonlinear analysis in the vicinity of this point to derive so-called amplitude equations which describe the evolution of patterns on large temporal and spatial scales. The amplitude dynamics of left and right traveling waves as well as the Turing pattern is captured in three mutually coupled complex Ginzburg–Landau equations. Numerical simulations of these equations and the coupled SHEs coincide, but the former provide substantially more insight into the coexistence of patterns. Each pattern locally suppresses other patterns and tends to saturate to a constant amplitude solution. In a certain range of parameters, both wave and Turing patterns are stable. In this bistable regime, random initial conditions typically result in the coexistence of different patterns in different spatial domains which are separated by distinct interfaces: wave-Turing interfaces as well as sources and sinks which separate left and right traveling waves, respectively. Now, the properties of these interfaces are pivotal for local control of globally competing patters: A small spatial dip in the scalar parameter mentioned above may pin these interfaces. Moving this dip shifts the interface position and results in the expansion of a pattern. As each type of interface has a different susceptibility to pinning, parameter dips of certain magnitudes pin interfaces selectively. Therefore, global control by local intervention can be achieved in the absence of spatial information.

DOI 10.20347/WIAS.PREPRINT.2457 Berlin 2017

1 Introduction

Pattern formation is one of the central topics in the study of physical systems far from thermodynamical equilibrium [4, 5]. Examples of nonequilibrium pattern formation have been reported in systems as diverse as hydrodynamic flows [35], chemical reactions [11], and ecosystems [20]. Recently, many studies have concentrated on biological patterns ranging from mechanochemical waves and protein patterns inside cells [3, 8] over tissue organization and morphogenesis [15, 31] to vegetation pattern [36].

Instabilities leading to such pattern formation can be classified in three types: (i) oscillatory in time and stationary in space, (ii) periodic in space and stationary in time or (iii) periodic in both space and time, which are referred to as Hopf, Turing, and wave instability [5]. The simultaneous occurrence of two instabilities is associated with a codimension-two bifurcation. In the vicinity of such a bifurcation interactions of the emerging patterns can be observed and the phenomenology gets increasingly rich. Out of all possible combinations the Hopf-Turing system has been studied most extensively, both experimentally and theoretically [6, 19, 28]. The other systems have been investigated to a lesser degree. Turing-Turing interactions have been suggested as a possible explanation for experimentally found superlattice hexagonal patterns [40] and are also subject of analysis in the modelling of dryland vegetation patterns [12]. Wave-Turing interactions were mainly studied in the context of a Belousov-Zhabotinsky reaction confined in a microemulsion [1, 2, 39].

The dynamics near codimension-two bifurcations are either constructive interactions, where new patterns are formed by resonant superpositions [40], or competing interactions, where the system exhibits multiple stable possibilities [25]. In the latter case it remains an open question how to actively manipulate patterns in order to select the desired one. Common concepts to control global system characteristics in pattern forming systems involve feedback with [9] or without delay [30], and global [23, 29] or local [26] spatiotemporal forcing.

Here we consider a generic model for competing wave and Turing patterns and show how to select between certain solutions by imposing local control on the system. We make use of the fact that competing patterns in large scale system occur in distinct spatial regions that are organized by the interfaces separating them. Those interfaces can be dragged, similarly to the position control of wave fronts [18], by local control. We explain the underlying mechanisms in terms of amplitude equations.

The model we study, which was proposed in [33], consists of two anti-symmetrically coupled Swift–Hohenberg equations (SHEs)

$$\partial_t u_1 = \eta u_1 - \left(1 + \partial_{xx}\right)^2 u_1 - u_1^3 - \alpha\, u_2 \tag{1a}$$

$$\partial_t u_2 = \eta u_2 - \left(1 + \mu^2 \partial_{xx}\right)^2 u_2 - u_2^3 + \alpha\, u_1\,, \tag{1b}$$

where η, α and μ are the control parameter of a single SHE, the coupling strength and the ratio of intrinsic wavenumbers of the individual equations, respectively.

The Swift–Hohenberg equation is a generic equation for a supercritical Turing instability. As such, it is used to model many physical, chemical and biological systems [17, 34]. The antisymmetric coupling of the equations breaks the variational nature of the single SHE and allows for oscillatory dynamics. More pictorially, the Turing patterns from the single equations are dragging each other due to the antisymmetric coupling, which results into traveling waves. The SHE captures only the essential characteristics that are necessary to generate Turing patterns. Thus, model (1) brings us close to a minimal system to study wave-Turing interaction.

There exist several mathematical papers that rigorously justify the Ginzburg–Landau equation as am-

plitude equation for the single Swift–Hohenberg equation, see e.g. [13, 21, 22]. To our best knowledge, all rigorous methods fail when two Swift–Hohenberg equations are coupled antisymmetrically, and, therefore, we formally justify our amplitude equations following e.g. [24].

The present paper is organized as follows: In Section 2 we briefly discuss the basic properties of the model's homogeneous steady state via linear stability analysis. In section 3 we derive amplitude equations for the systems and use them to identify the main features that govern the system's dynamics. Sections 4.1 and 4.2 cover the control of competition between wave-wave and wave-Turing patterns, respectively. Section 5 is devoted to concluding and discussing the results. In the appendix we carry out the linear stability analysis and the derivation of the amplitude equations in more detail.

2 Linear stability analysis

For all parameter values, Eq. (1) exhibits the homogeneous fixed point $(0,0)^\top$, for which we perform linear stability analysis, see appendix A. For a fixed ratio of intrinsic wavelengths μ, with $0<\mu<1$, it reveals two supercritical bifurcations: a Turing instability and a wave instability, whose bifurcation lines are intersecting at a codimension-two bifurcation point, given by

$$\eta_\mathrm{c} = \frac{(1-\mu^2)^2}{2\,(1+\mu^4)}\,, \tag{2a}$$

$$\alpha_\mathrm{c} = \sqrt{-\left(\eta_\mathrm{c}-(1-k_\mathrm{T}^2)^2\right)\left(\eta_\mathrm{c}-(1-\mu^2k_\mathrm{T}^2)^2\right)}, \tag{2b}$$

where k_T is the critical wavenumber of the Turing instability, implicitly given in Eq. (34). Analogously, the critical wavenumber of the wave instability is detailed in Eq. (33). The linear stability diagram, which is qualitatively invariant for different values of μ, is shown in Fig. 1 for $\mu=1/2$. The stability behavior of the two limit cases $\mu\to 1$ and $\mu\to 0$ can be deduced from Eqs. (2): The former case results in $\eta_\mathrm{c}\to 0$ and a wave bifurcation only, which evolves as the two identical Turing modes of the single SHEs are dragging each other. As $\mu\to 0$, $\alpha_\mathrm{c}\to\infty$ and the wave instability vanishes. This can be rationalized by the scale separation of the two Turing patterns. Note that our results displayed in Fig. 1 differ in some aspects from the linear stability diagram given in [33]: The maxima of the dispersion relation related to the wave instability and a long-wavelength Turing instability do not coincide. Thus, there exists a parameter regime in which three patterns could potentially get unstable.

3 Weakly nonlinear analysis

3.1 Amplitude equations

Passing through the codimension-two bifurcation point from the regime where the homogeneous solution is stable, Turing and wave patterns become unstable simultaneously. Near this point we can expect both patterns to be relevant for the system dynamics. In order to study possible interactions, we perform weakly nonlinear analysis, making use of the amplitude equation formalism [5, 10]. We introduce a formal perturbation ansatz for $\boldsymbol{u}=(u_1,u_2)^\top$ with $\eta=\eta_\mathrm{c}+\varepsilon^2\eta_\mathrm{p}$ and $\alpha=\alpha_\mathrm{c}+\varepsilon^2\alpha_\mathrm{p}$,

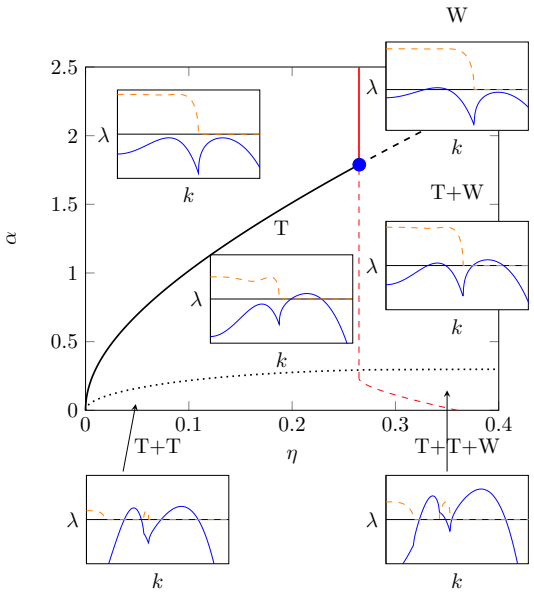

Figure 1: Linear stability diagram of the homogeneous state $(0,0)^\top$ for $\mu = 1/2$. The solid red and black lines represent supercritical wave and Turing bifurcations, respectively. The dashed red and black lines indicate regions of wave and Turing instabilities, respectively, see appendix A for details. The dotted black line indicates the instability of a second Turing pattern with larger wavelength, which originates from Eq. (1b). The subfigures show the real (solid blue line) and imaginary (dashed orange line) part of the characteristic dispersion relation for different parameter regions. Their headline denote corresponding instabilities.

where $0 < \varepsilon \ll 1$

$$\begin{aligned}\boldsymbol{u}(t,x) = \varepsilon \mathrm{Re}\,\big[&A_\mathrm{L}(\varepsilon t, \varepsilon^2 t, \varepsilon x, \varepsilon^2 x) e^{i(k_\mathrm{W} x + \omega t)} \boldsymbol{u}_\mathrm{L} \\ &+ A_\mathrm{R}(\varepsilon t, \varepsilon^2 t, \varepsilon x, \varepsilon^2 x) e^{i(k_\mathrm{W} x - \omega t)} \boldsymbol{u}_\mathrm{R} \\ &+ A_\mathrm{T}(\varepsilon t, \varepsilon^2 t, \varepsilon x, \varepsilon^2 x) e^{i(k_\mathrm{T} x)} \boldsymbol{u}_\mathrm{T}\big] \\ &+ \varepsilon^2 \boldsymbol{u}_2 + \varepsilon^3 \boldsymbol{u}_3 + \mathcal{O}(\varepsilon^4)\,.\end{aligned} \tag{3}$$

Thus, we expand the model variables in terms of complex amplitudes of the three linearly unstable modes at the codimension-two point: left traveling waves A_L, right traveling waves A_R, and Turing patterns A_T. This ansatz is inserted into Eq. (1), setting the slow scales $\chi_1 = \varepsilon x$, $\chi_2 = \varepsilon^2 x$, $\tau_1 = \varepsilon t$, $\tau_2 = \varepsilon^2 t$ and sorting in powers of ε. Assuming that secular terms of the resulting equations vanish, one finds the following solvability conditions of order ε^2

$$\begin{aligned}(\partial_{\tau_1} - c\partial_{\chi_1}) A_\mathrm{L}^* &= 0 \\ (\partial_{\tau_1} + c\partial_{\chi_1}) A_\mathrm{R}^* &= 0\end{aligned} \tag{4}$$

and of order ε^3

$$\begin{aligned}(\partial_{\tau_2} - c\partial_{\chi_2}) A_\mathrm{L}^* &= \kappa_\mathrm{W} A_\mathrm{L}^* + D_\mathrm{W} \partial_{\chi_1\chi_1} A_\mathrm{L}^* + \sigma_\mathrm{W} |A_\mathrm{L}^*|^2 A_\mathrm{L}^* \\ &\quad + \sigma_\mathrm{WW} |A_\mathrm{R}^*|^2 A_\mathrm{L}^* + \sigma_\mathrm{WT} |A_\mathrm{T}^*|^2 A_\mathrm{L}^* \\ (\partial_{\tau_2} + c\partial_{\chi_2}) A_\mathrm{R}^* &= \overline{\kappa}_\mathrm{W} A_\mathrm{R}^* + \overline{D}_\mathrm{W} \partial_{\chi_1\chi_1} A_\mathrm{R}^* + \sigma_\mathrm{W} |A_\mathrm{R}^*|^2 A_\mathrm{R}^* \\ &\quad + \sigma_\mathrm{WW} |A_\mathrm{L}^*|^2 A_\mathrm{R}^* + \overline{\sigma}_\mathrm{WT} |A_\mathrm{T}^*|^2 A_\mathrm{R}^* \\ \partial_{\tau_2} A_\mathrm{T}^* &= \kappa_\mathrm{T} A_\mathrm{T}^* + D_\mathrm{T} \partial_{\chi_1\chi_1} A_\mathrm{T}^* + \sigma_\mathrm{T} |A_\mathrm{T}^*|^2 A_\mathrm{T}^* \\ &\quad + \sigma_\mathrm{TW} |A_\mathrm{L}^*|^2 A_\mathrm{T}^* + \sigma_\mathrm{TW} |A_\mathrm{R}^*|^2 A_\mathrm{T}^*\,.\end{aligned} \tag{5}$$

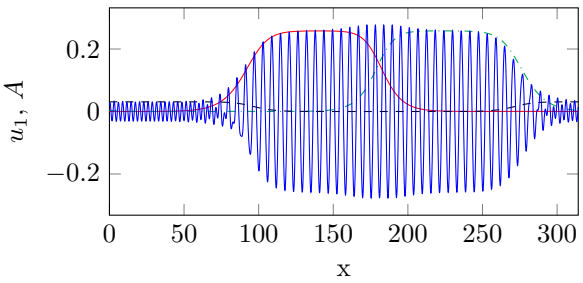

Figure 2: Numerical comparison of the SHEs (1) and the amplitude Eqs. (6) with corresponding initial conditions after t=200. u_1 is shown as blue solid line, $u_{\mathrm{T}}^1|A_{\mathrm{T}}|$, as dashed black line, $u_{\mathrm{W}}^1|A_{\mathrm{L}}|$ as red solid line and $u_{\mathrm{W}}^1|A_{\mathrm{R}}|$ as green dash-dotted line. Simulations were performed at $\alpha = \alpha_{\mathrm{c}}$, $\eta = \eta_{\mathrm{c}} + 0.05$ and $\mu = 0.5$ with periodic boundary conditions. See also video 1 in the supplementary material for the whole simulation.

The coefficients admit closed form expressions that are given in Appendix B alongside a more detailed derivation of the equations in (4)–(5). For the understanding of the following it suffices to know that the coefficients κ_{W}, D_{W} and σ_{WT} are complex while the other coefficients are real valued. All the coupling coefficients σ_i have negative real parts. Considering that the solvability conditions yield a system of evolution equations for the amplitudes, negativity of the coupling coefficients corresponds to local mutual suppression of the different patterns.

System (4)-(5) consists in total of five equations in four different variables. This is quite impractical for further numerical and analytical computations. In the literature several ways are discussed to simplify such systems [14]. We make use of the method of reconstitution. We reconstitute the original scales (t, x) and multiply Eqs. (4)-(5) with the corresponding order of ε^2 and ε^3, respectively. Adding them up results in a reduced system of coupled complex Ginzburg–Landau equations (CGLE)

$$\begin{aligned}
(\partial_t - c\partial_x)A_{\mathrm{L}} &= \varepsilon^2\kappa_{\mathrm{W}}A_{\mathrm{L}} + D_{\mathrm{W}}\partial_{xx}A_{\mathrm{L}} + \sigma_{\mathrm{W}}|A_{\mathrm{L}}|^2A_{\mathrm{L}} \\
&\quad + \sigma_{\mathrm{WW}}|A_{\mathrm{R}}|^2A_{\mathrm{L}} + \sigma_{\mathrm{WT}}|A_{\mathrm{T}}|^2A_{\mathrm{L}} \\
(\partial_t + c\partial_x)A_{\mathrm{R}} &= \varepsilon^2\bar{\kappa}_{\mathrm{W}}A_{\mathrm{R}} + \overline{D}_{\mathrm{W}}\partial_{xx}A_{\mathrm{L}} + \sigma_{\mathrm{W}}|A_{\mathrm{R}}|^2A_{\mathrm{R}} \\
&\quad + \sigma_{\mathrm{WW}}|A_{\mathrm{L}}|^2A_{\mathrm{R}} + \overline{\sigma}_{\mathrm{WT}}|A_{\mathrm{T}}|^2A_{\mathrm{R}} \\
\partial_t A_{\mathrm{T}} &= \varepsilon^2\kappa_{\mathrm{T}}A_{\mathrm{T}} + D_{\mathrm{T}}\partial_{xx}A_{\mathrm{T}} + \sigma_{\mathrm{T}}|A_{\mathrm{T}}|^2A_{\mathrm{T}} \\
&\quad + \sigma_{\mathrm{TW}}|A_{\mathrm{L}}|^2A_{\mathrm{T}} + \overline{\sigma}_{TW}|A_{\mathrm{R}}|^2A_{\mathrm{T}}\,,
\end{aligned} \tag{6}$$

where $A_k(t,x) = A_k^*(\varepsilon t, \varepsilon^2 t, \varepsilon x, \varepsilon^2 x) + O(\varepsilon^4)$ for $k \in \{\mathrm{L}, \mathrm{R}, \mathrm{T}\}$. Using the CGLE for modeling the amplitude behavior of counterpropagating wave systems is a common approach and it often yields qualitative correct behavior [37]. In particualr, as $\varepsilon \to 0$ they are again described by Eqs. (4)-(5). Nevertheless they are not the asymptotically correct amplitude equations and therefore careful comparison with the underlying SHEs has to be done. See [14] for a detailed discussion of this issue.

As for this work, the analytical results presented in subsection 3.2 are also valid for the system (4)-(5), while the numerics were performed using the reduced equations (6). Numerical results of the amplitude equations will be validated by direct numerical integration of the underlying SHEs (1). To put this into context and motivate the validity for finite ε, Fig. 2 shows a direct comparison between SHEs (1) and the reduced amplitude equations (6) at a distance from the codimension-two point of $\alpha - \alpha_{\mathrm{c}} = 0$ and $\eta - \eta_{\mathrm{c}} = 0.05$. Apparently, the amplitude equations approximate the envelope of the patterns that evolve in simulations of the SHEs very well, both qualitatively and quantitatively. These solutions also exhibit the basic structures of patterns in the weakly nonlinear regime of the SHEs. The amplitude equations reveal that the evolution of the different modes is mainly governed by linear

driving associated with κ_{W} and κ_{T}, diffusion with constants D_{W} and D_{T} and negative cubic coupling with coupling coefficients σ_i. Small initial perturbations in single modes will therefore grow through linear driving and spread due to diffusion into the whole domain until the nonlinearity balances out the growth. This leads to constant amplitude solutions that are discussed in Sec. 3.2.

In the case that perturbations in different modes occur a single system they will start to spread individually until they suppress each other due to cubic interaction. This local mutual suppression results into a situation where patches of different patterns exist in the system connected by localized interfaces as in Fig. 2. We further characterize those interface solutions in Sec. 3.4.

3.2 Constant amplitude solutions and secondary instabilities

As stated before, single patterns tend to saturate to constant amplitude solutions. In terms of amplitude equations these states balance the linear driving terms associated with κ_{T} and κ_{W}, and the saturation terms associated with σ_{T} and σ_{W}. They can be written as:

$$A_{\mathrm{L}} = \rho_{\mathrm{W}} e^{i(\Omega_{\mathrm{W}} t + p_{\mathrm{L}} x)}, \quad A_{\mathrm{R}} = 0, \quad A_{\mathrm{T}} = 0\,, \tag{7}$$

$$A_{\mathrm{L}} = 0, \quad A_{\mathrm{R}} = \rho_{\mathrm{W}} e^{i(-\Omega_{\mathrm{W}} t + p_{\mathrm{R}} x)}, \quad A_{\mathrm{T}} = 0\,, \tag{8}$$

$$A_{\mathrm{L}} = 0, \quad A_{\mathrm{R}} = 0 \quad A_{\mathrm{T}} = \rho_{\mathrm{T}} e^{i p_{\mathrm{T}} x}\,. \tag{9}$$

with

$$\rho_{\mathrm{W}}^2 = -\frac{\mathrm{Re}\left[\varepsilon^2 \kappa_{\mathrm{W}} - p_{\mathrm{L/R}}^2 D_{\mathrm{W}}\right]}{\sigma_{\mathrm{W}}} \tag{10}$$

$$\Omega_{\mathrm{W}} = \left(\mathrm{Im}\left[p_{\mathrm{L/R}}^2 D_{\mathrm{W}} + \varepsilon^2 \kappa_{\mathrm{W}}\right] + p_{\mathrm{L/R}} c\right) \tag{11}$$

$$\rho_{\mathrm{T}}^2 = -\frac{\varepsilon^2 \kappa_{\mathrm{T}} - p_{\mathrm{T}}^2 D_{\mathrm{T}}}{\sigma_{\mathrm{T}}}\,. \tag{12}$$

The free parameters $p_{\mathrm{L}}, p_{\mathrm{R}}$ and p_{T} denote the deviation of the particular pattern's wavelength from their critical values at the codimension-two point. ρ_{L}, ρ_{R} and ρ_{T} are the saturated amplitudes, while Ω_{L} and Ω_{R} denote corrections to the waves phase velocities. In order to further understand the system's behavior, stability analysis of the constant amplitude solutions is performed. It turns out that saturated Turing patterns are unconditionally stable, if the criterion

$$\mathrm{Re}\left[\varepsilon^2 \kappa_{\mathrm{W}} + \rho_{\mathrm{T}}^2 \sigma_{\mathrm{WT}}\right] < 0 \tag{13}$$

holds. This can be expressed in terms of the original model parameters as $\alpha < \alpha_{\mathrm{c}}$. If Eq. (13) is not fulfilled, the fixed point gets unstable with respect to perturbations of the traveling wave amplitudes A_{L} and A_{R}. Constant amplitude wave solutions on the other hand are stable, if

$$\mathrm{Re}\left[\varepsilon^2 \kappa_{\mathrm{T}} + \rho_{\mathrm{W}}^2 \sigma_{\mathrm{TW}}\right] < 0\,. \tag{14}$$

Otherwise there is an instability with respect to perturbations in the Turing amplitude. Eq. (14) can be rewritten as

$$\alpha - \alpha_{\mathrm{c}} < \frac{\alpha_{\mathrm{c}}^2 - a_{\mathrm{T}}^2}{2\alpha_{\mathrm{c}} a_{\mathrm{T}}} (\eta - \eta_{\mathrm{c}})\,, \tag{15}$$

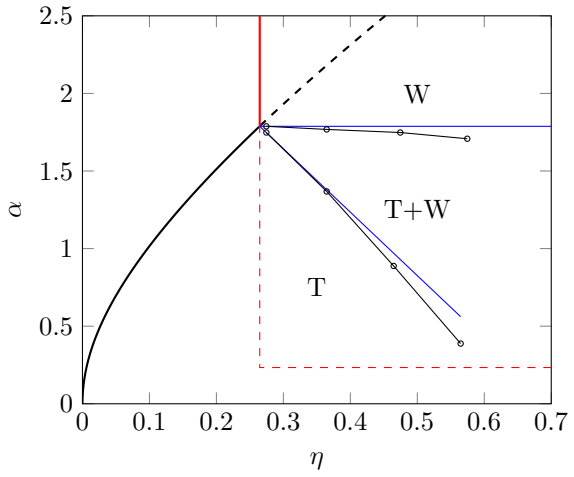

Figure 3: Phase diagram of the coupled SHEs for $\mu = 0.5$. Alongside the Turing and wave bifurcations that are shown in the same way as in Fig. 1 secondary bifurcations of plain waves and Turing patterns are shown. Blue lines indicate the stability criterion derived from the amplitude equations, see Eqs. (13) and (14). Black circles are calculated by integrating the SHEs (1). For fixed values of η, several simulations were run starting from either plain waves or Turing patterns for t=20000 each. The value of α was changed iteratively in multiple simulations which used the final state of the last simulation as initial conditions until a change of the patterns occurred. Black circles indicate the last parameter combination where no change of pattern was observed.

where we introduced $a_\mathrm{T} = \eta_\mathrm{c} - (1 - k_\mathrm{T}^2)^2$ for easier notation. The system's stability is not further limited by sideband instabilities as the Benjamin–Feir or the Eckhaus instability. For waves we find that

$$\sigma_\mathrm{W} \left(D_\mathrm{W} + \overline{D}_\mathrm{W} \right) = -3\alpha_\mathrm{c}^2 (1 + \mu^2) < 0 \tag{16}$$

is satisfied unconditionally, which corresponds to the Benjamin–Feir criterion. Similarly for Turing patterns it holds that $\sigma_\mathrm{T} D_\mathrm{T} < 0$. Therefore there is no Eckhaus instability.

Eqs. (7)–(9) are not the only constant amplitude fixed points of the amplitude equations. Also combinations of constant amplitudes, such as standing waves (combination of left and right traveling waves) or wave-Turing mixed states can be considered. The corresponding stability criterion for standing waves (wave-wave mixed states) is given by

$$\sigma_\mathrm{W} \pm \sigma_\mathrm{WW} < 0\,. \tag{17}$$

As $\sigma_\mathrm{W} + \sigma_\mathrm{WW} > \sigma_\mathrm{W} - \sigma_\mathrm{WW} = \frac{3}{4}\alpha_\mathrm{c}^2 > 0$, this is never satisfied and standing waves are always unstable with respect to single traveling wave amplitudes. The remaining criteria of other mixed states get highly intricate. Thus we draw on numerical simulations of the amplitude equations. There mixed states did not appear. Therefore we expect they are not stable. This behavior is also in line with our perspective of mutually suppressing amplitudes.

3.3 Bistability

From the stability considerations above, we derived the phase diagram, see Fig. 3, which exhibits overlapping stability regions of traveling waves and Turing patterns, resulting in a bistable regime. The phase diagram stays qualitatively invariant for all μ. The predicted bistable regime was validated

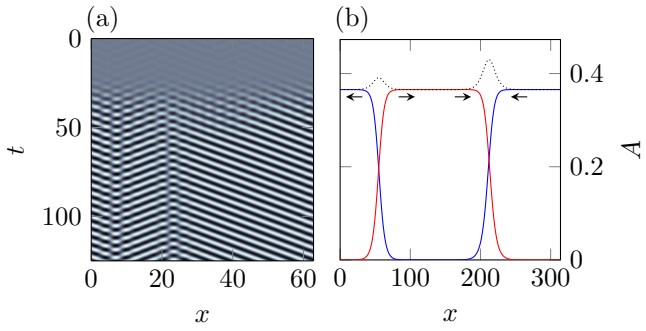

Figure 4: Two counterpropagating waves separated by a source and a sink. (a) Space-time plot of u_2 obtained by numerical integration of the SHEs (1). Parameters are $\eta = \eta_c + 0.3, \alpha = \alpha_c, \mu = 0.5$. (b) Result from numerical integration of the amplitude equations (6). $|A_L|$ and $|A_R|$ in solid blue and red line, respectively, while $|A_L + A_R|$ is depicted as dotted black line. Parameters are $\eta = \eta_c + 0.1$, $\alpha = \alpha_c$ and $\mu = 0.5$. Arrows indicate the direction of the group velocity of the respective traveling wave.

numerically by integrating Eq. (1), see Fig. (3). The numerically calculated region of bistability is in good agreement with the analytical predictions of Eqs. (13) and (14) near the codimension-two point. At larger distance to this point nonlinear effects become important, such that the bifurcation lines start to differ.

Overall, Eq. (1) exhibit two kinds of bistability: (i) bistability of left and right traveling waves that all traveling wave systems with spatial reflection symmetry share and (ii) bistability of Turing and wave patterns that is discussed above.

3.4 Sources, sinks, and wave-Turing interfaces

We have pointed out parameter regimes for which different patterns can not only emerge from the homogeneous state, but their saturated states are also stable. The situation gets more complicated if the initial conditions are such that different patterns are evolving in different spatial regions.

Eventually the patterns will compete for the same space, since mixed states are not stable. Because of local mutual suppression they cannot penetrate each other and localized interfaces are forming that connect individual patches of saturated patterns, see Fig. 2.

Interfaces between left and right travelling waves are categorized with respect to the directions of the associated group velocities: Interfaces at which group velocities of the two patterns are pointing outwards of the interface are called sources, interfaces at which group velocities are pointing inwards are called sinks [37]. It turns out that the interfaces can be distinguished by the sum of amplitudes, see Fig. 4(b). Sinks exhibit a higher sum of amplitudes as they are pushed together by the group velocities, while sources are pulled apart.

As for Eqs. (1) the definition of sources and sinks coincides with phase sources and sinks, respectively. This is because group and phase velocity point in the same direction (which has not to be true in general [37]). Fig. 4(a) therefore displays a sink on the left and a source on the right. In numerical simulations sources and sinks were always found to be reflection symmetric with respect to space and therefore stationary.

The second type of interface that can be found near the codimension-two point of Eqs. (1) is the wave-

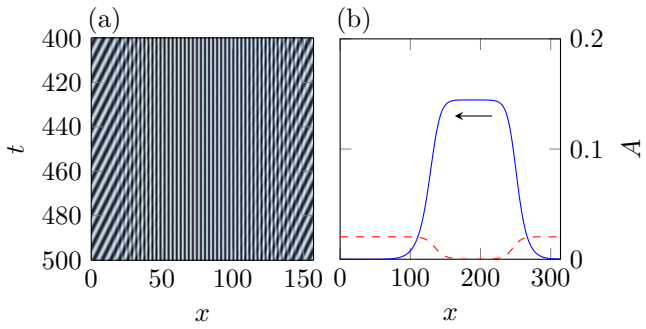

Figure 5: A Turing pattern and a left traveling wave separated by wave-Turing interfaces. (a) Space time plot of u_2 obtained by numerical integration of the SHEs (1) at parameter values $\eta = \eta_c + 0.1$, $\alpha = \alpha_c - 0.1$ and $\mu = 0.5$. (b) Results from the amplitude equations (6) at parameter values $\eta = \eta_c + 0.05$, $\alpha = \alpha_c - 0.05$ and $\mu = 0.5$. $u_W^1|A_L|$ as solid blue and $u_T^1|A_T|$ as dashed red line. The arrow indicates the direction of the group velocity of the left traveling wave.

Turing interface, see Fig. 5. Wave-Turing interfaces are naturally asymmetric and thus not stationary. Instead, they move at constant speed. Because this movement is on the scale of the group velocities and therefore way slower than the phase velocities of the wave patterns, this behavior is hardly recognizable in Fig. 5(a).

Similarly to the wave-wave case, we can categorize wave-Turing interfaces depending on the wave's group velocity into inward interfaces for which the wave's group velocity points into the direction of the interfaces and outward interfaces where it points outwards, see Fig. 5(b) with an inward interface on the left and an outward interface on the right. In weakly nonlinear regimes, inward and outward interfaces will typically move in the direction of the wave's group velocity, but with different velocities, resulting in shrinking and growing wave or Turing patches. In strongly nonlinear regimes, the patch widths can stabilize by phase locking [25].

4 Position control of interface solutions

In the last section we showed that the competition of different patterns in regimes of bistability of the SHEs (1) can be governed by interfaces separating different patterns. As they can occur by chance due to random initial perturbations of the homogeneous state, one can actually be sure to find different patterns in one system, if the domain size is chosen large enough. Movement of the interfaces can lead to shrinking up to vanishing of certain pattern patches. Thus by controlling the position of the interfaces we can select between different patterns in one system. For example if we moved the source in Fig. 4(b) to the right, letting it annihilate with the sink, the whole domain would be governed by left traveling waves. If there was another source to the right of the sink (or we simply use periodicity of the simulation domain) and we move it to the left we would end up with right traveling waves. To establish such position control we introduce space and time dependent parameters

$$\begin{aligned} \alpha(t,x) &= \alpha_c + \varepsilon^2 \alpha_p(t,x) \\ \eta(t,x) &= \eta_c + \varepsilon^2 \eta_p(t,x)\,. \end{aligned} \tag{18}$$

Under the assumption that the parameters change slowly in time and space, the amplitude equations stay as they are, while κ_W and κ_T inherit the space and time dependence. They can be computed by inserting the space and time dependant α_p and η_p into Eq. (45). In particular we observe that

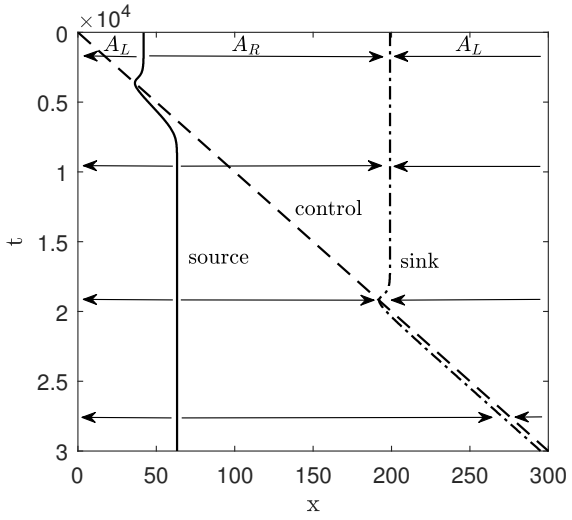

Figure 6: Space time plot of position control of the amplitude equations with one source and one sink at $\hat{\eta}_\mathrm{p} = 0.1$ and $\alpha = \alpha_\mathrm{c}$. The control parameters are $\hat{\eta}_\mathrm{c} = -0.014$, $b_\eta = 4$ and $v_\mathrm{c} = 0.01$. The control signal, whose position is indicated by the dashed line, moves through the domain. While the position of the source (solid line) is only manipulated slightly, the sink (dash dotted line) pins to the control and follows it. Arrows indicate the direction of the group velocities of the wave patches.

$\mathrm{Re}[\kappa_\mathrm{W}](t,x) \propto \eta_\mathrm{p}(t,x)$ and $\mathrm{Im}[\kappa_\mathrm{W}](t,x) \propto \alpha_\mathrm{p}(t,x)$, while κ_T is linear in both η_p and α_p. If the parameters change rapidly, nonadiabatic corrections to the amplitude equations have to be taken into account, cf. [27].

Throughout this paper we use Gaussian control in η of the kind

$$\eta_\mathrm{p}(t,x) = \hat{\eta}_\mathrm{p} + \hat{\eta}^\mathrm{cont} e^{-\frac{(x - v^\mathrm{cont} t)^2}{b_\eta}} \tag{19}$$

with constant control velocity v_c. Fig. 8 shows that different control shapes lead qualitatively to the same effects.

4.1 Control of sources and sinks

The above considerations lead us to the most straightforward way for position control of interfaces. We use pinning of sources and sinks to the control signal in Eq. (19), see Fig. 6. In the displayed simulation the control signal is moved through the domain first hitting the source. Although the source follows the control for some time, it is not completely pinned. Stronger control is necessary for that. The sink on the other hand gets pinned and follows the control the whole way. The reasons and consequences of the different affinity of sources and sinks to control in η are explained in the following.

Pinning of localized structures to inhomogeneities is a well known effect, see [7, 38] and references therein. In this work we do not investigate fully nonlinear pinning effects, as most works deal with, but weakly nonlinear ones, which can be explained in terms of amplitude equations.

In Fig. 7 the pinning mechanism of a sink to a negative Gaussian inhomogeneity is displayed. Moving with constant speed v^cont to the right, it enters the sink until it hits the left traveling wave front slightly right to the sink's center. Since η is locally lower at this point, also κ_W, which is related to the fact that linear driving of the amplitude equations is lower. Thus the amplitudes are locally suppressed (or less enhanced to be more precise). Right from the sinks center the effect on the left traveling wave

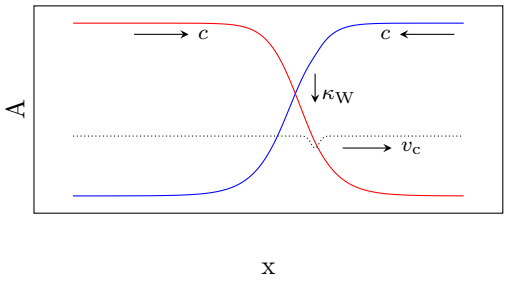

Figure 7: Pinning mechanism of a sink to a dip in the parameter η. Right (left) traveling wave in red (blue) solid line, η_p in dotted black line.

is stronger, since it possesses a larger amplitude. The suppression of the left traveling wave makes room for the right traveling wave to advance. If the control signal is strong and moving slow enough, the sink will thus follow it. This pinning mechanism is also applicable to sources.

From the above mechanism it follows that sinks are easier to pin than sources. In the case of a sink, once one amplitude gets suppressed by the control, the other front is faster to move into the freed space, because its group velocity is pointing inside the sink. In the case of sources it is slower, because the group velocity is pointing outwards of the source. See also video 2 from supplementary for an example with different pinning strengths.

We investigate the pinning behavior by numerically integrating the amplitude equations with two different control signal shapes (Gaussian and rectangular) and different width to height ratios, as well as with varying control velocities at constant widths. From the scaling behavior of the pinning strength depicted in Fig. 8 we can deduce further insights about the pinning mechanisms. First of all, a smaller control signal is sufficient to pin sinks than to pin sources. In this context for equal control width and velocity, the respective height parameter ($\hat{\eta}^{\mathrm{cont}}$ for gaussian signal, signal height for rectangular signal) is lower at pinning onset. This effect is independent of control shape and velocity. Moreover, for small signal widths the area under the control signal is a constant at the pinning threshold, seemingly independent from the signal shape. From some characteristic width upwards, larger control signals are needed. Similar behavior can be observed for the pinning of fronts to inhomogeneities, cf. [16]. There the pinning is governed by the convolution of the parameter inhomogeneity with the Goldstone mode of the front.

The fact that sinks are easier to pin than sources gives us a mechanism at hand to select between left and right traveling waves. Using a control signal in the intermediate regime which is pinning sinks but not sources, we can select between left and right traveling waves by choosing the movement direction of the control signal. Starting the signal at the left side of the domain, moving it to the right, it will ignore sources and pin the first sink. Thus the right traveling front is pulled through the system. In case of a periodic system, it will be governed by right traveling waves completely afterwards. Choosing a left moving control selects left traveling waves. See video 3 from supplementary material for an illustration.

The described protocol allows for global pattern selection with a local control, without knowledge of the exact locations of sources and sinks, they only have to exist. The main result of this section, namely that there is a certain interval in which control works for sinks but not for sources was confirmed by direct numerical integration of the coupled SHEs (1).

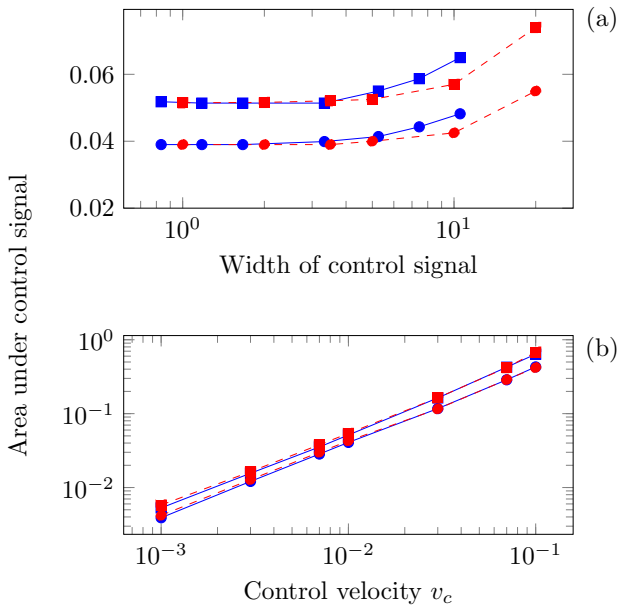

Figure 8: Effectiveness of pinning. Squares refer to the pinning of sources, circles to the pinning of sinks. Solid blue lines denote Gaussian control and red dashed lines rectangular shaped control. Results were obtained by numerically integrating Eqs. (6) at parameters $\hat{\eta}_\mathrm{p} = 0.05$, $\alpha = \alpha_\mathrm{c}$ and $\mu = 0.5$. (a) At constant $v^\mathrm{cont} = 0.01$ and different constant widths (full width for rectangular control, full width at half height for Gaussian) the control signal height was varied until onset of pinning. (b) At constant width b_η of 4 and 3.33 for rectangular and Gaussian control, respectively, for different constant control velocities the control height was varied until pinning onset.

4.2 Control of wave-Turing interfaces

Again, we use the signals in Eq. (18) to control the wave-Turing interfaces, as we did for the wave-wave interfaces. The mechanisms work slightly different though. In contrast to left and right traveling waves, which only differ with respect to the sign of their phase and group velocity, but not their stability behavior, Turing and wave patterns are reacting differently to changes in η. We showed before, that weakly nonlinear pinning to parameter inhomogeneities can be explained with changes in the real parts of linear driving coefficients κ_W and κ_T. We can interpret those real parts geometrically in terms of the perpendicular distance of a parameter point to the bifurcation line in parameter space. Fig. 1 thus shows, that the sensitivity of the real part of κ_W is larger than that of κ_T with respect to η.

Positive or negative inhomogeneities in η thus locally support the wave or the Turing front, respectively. This can stop the natural movement of the interface or impose an artificial one. In the part of the bistable regime, where interfaces move in the same direction as the wave's group velocity we use stationary control signals either to stop the movement of the inward or the outward interface. As shown and discussed in Fig. 9 outward interfaces can be pinned by positive and inward interfaces by negative control signals. Having the knowledge whether left or right traveling waves are present in the system, thus enables us to select between wave and Turing patterns, see also video 4 in the supplementary material. Necessary for that is that the desired pattern does not vanish by natural pattern patch shrinking before the relevant interfaces can be pinned.

Pinning of outward and inward interfaces with positive and negative control signals has been confirmed by numerical integration of Eqs. (1).

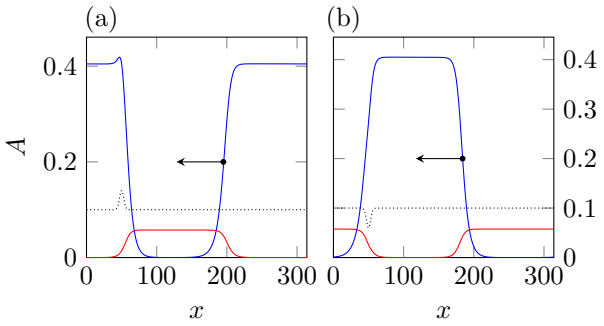

Figure 9: Pinning of wave-Turing interfaces in two simulations of Eq. (6) with identical initial conditions. $u^1_{\mathrm{W}}|A_{\mathrm{L}}|$ ($u^1_{\mathrm{T}}|A_{\mathrm{T}}|$) denoted by blue(red) line, η_{p} by black dotted line. Parameters are $\alpha = \alpha_{\mathrm{c}} - 0.3$, $\mu = 0.5$. (a) Pinning of an outward interface by positive control. Without control, the interface would move to the left as a result from the left pointing group velocity. The local enhancement of the wave stops the wave from retreating form the interface and pins it. (b) Pinning of an inward interface by negative control. This time the pinning works by locally suppressing the wave front to advance to the left.

5 Conclusion

We investigated the competition and control of patterns in a system of two anti-symmetrically coupled Swift–Hohenberg equations. Linear stability analysis revealed the existence of a codimension-two bifurcation point, where wave and Turing patterns occur simultaneously. By performing weakly nonlinear analysis in vicinity of this point, we derived coupled amplitude equations for the dynamics and interaction of these patterns. The mutual suppression of amplitudes of Turing and wave patterns results in their bistability. Similarly, we find that right-traveling wave modes suppress left-traveling modes and vice versa leading to traveling waves instead of standing waves. Consequently, different stable patterns can appear in distinct spatial regions separated by localized interfaces. Rigorous justification of complex Ginzburg–Landau equations as amplitude equations failed due to the oscillatory dynamics of antisymmetrically coupled SHEs. Therefore we restrict ourselves to a formal derivation. However, we point out that the formal derivation may potentially be misleading as is shown in [32] for the Newell–Whitehead equation. Therefore, we have performed extensive numerical simulations to verify our findings.

Pinning of such interfaces to parameter inhomogeneities allows for efficient control of the interface positions. Certain choices of the parameters of the control signals are found to yield a selective pinning of interfaces. A particular size of the control signal pins for example only wave sinks but not sources. In the Turing-wave case, the sign of the control determines whether inward or outward interfaces are pinned. In the bistable parameter regime, a system always forms these interfaces, provided that the domain size is large enough. Thus, the presented control method allows for global pattern selection through local control.

While a single SHE is a model for the formation of stationary patterns in non-equilibrium systems, two anti-symmetrically coupled SHEs may be considered as a simple generic model for competing Turing and wave patterns. Therefore, our control scheme is rather general and applicable to a large variety of systems.

Supplementary material

Video 1 shows the numerical comparison of the SHEs (1) and the amplitude equations (6) with corresponding initial condition. See Fig. 2 for the simulation parameters.

Video 2 shows pinning in a system with one source and one sink with different control strengths $\hat{\eta}_\mathrm{c}$. From top to bottom there is (i) no pinning at all, (ii) pinning of sink only and (iii) pinning of the first interface that is hit by the control. Parameters are $\hat{\eta}_\mathrm{p} = 0.1$, $\alpha = \alpha_\mathrm{c}$. Control is at $v^\mathrm{cont} = 0.01$ and $b_\eta = 4$. The amplitude of the left traveling waves is shown in blue, the amplitude of right traveling waves in red, such that in the beginning there is a source at the left and a sink at the right.

Video 3 shows selection of right (top) marked by a red line and left (bottom) traveling waves marked by a blue line with a right and left moving control, respectively. Pinning strength is chosen such that only sinks are pinned. Parameters are $\hat{\eta}_\mathrm{p} = 0.1$, $\alpha = \alpha_\mathrm{c}$. Control is at $\hat{\eta}^\mathrm{cont} = 0.014$, $v^\mathrm{cont} = 0.01$ and $b_\eta = 4$.

Video 4 shows selection of left traveling wave (top) and Turing (bottom) patterns by positive and negative stationary control. Parameters are $\hat{\eta}_\mathrm{p} = 0.1$, $\hat{\alpha} = -0.3$. Control is at $\hat{\eta}^\mathrm{cont} = \pm 0.04$, $v^\mathrm{cont} = 0$ and $b_\eta = 15$.

A Linear stability analysis

We carry out a linear stability analysis of the uniform fixed point $(0,0)^\top$ of Eqs. (1). Employing the ansatz $\boldsymbol{u} = \boldsymbol{\delta}\, e^{ikx+\lambda t}$, we find the Jacobian

$$L(k) = \begin{pmatrix} f_1(k) & -\alpha \\ \alpha & f_2(k) \end{pmatrix}, \tag{20}$$

and the dispersion relation

$$\lambda(k) = \frac{f_1(k)+f_2(k)}{2} \pm \sqrt{\left(\frac{f_1(k)-f_2(k)}{2}\right)^2 - \alpha^2}\,, \tag{21}$$

where $f_1(k) = \eta - (1-k^2)^2$ and $f_2(k) = \eta - (1-\mu^2 k^2)^2$. For $\alpha > 0$, Turing and wave instabilities exist in different regions of wave number k. We analyze the root term in Eq. (21) to distinguish these cases which are independent of η. For $\alpha \leq (1-\mu^2)/(2\,(1+\mu^2))$, waves may emerge for k for which $0 < k < k_\mathsf{A}$ or $k_\mathsf{B} < k < k_\mathrm{c}$ hold, while Turing patterns may emerge for the other values of $k > 0$. The separating wave numbers k_A, k_B and k_c are given by

$$k_\mathsf{A} = \sqrt{\frac{1}{1+\mu^2} - \sqrt{\frac{1}{(1+\mu^2)^2} - \frac{2\,\alpha}{1-\mu^4}}}\,, \tag{22}$$

$$k_\mathsf{B} = \sqrt{\frac{1}{1+\mu^2} + \sqrt{\frac{1}{(1+\mu^2)^2} - \frac{2\,\alpha}{1-\mu^4}}}\,, \tag{23}$$

$$k_\mathrm{c} = \sqrt{\frac{1}{1+\mu^2} + \sqrt{\frac{1}{(1+\mu^2)^2} + \frac{2\,\alpha}{1-\mu^4}}}\,, \tag{24}$$

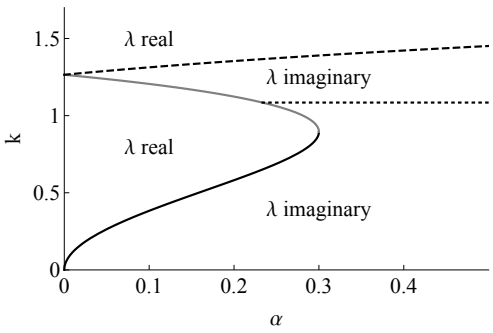

Figure 10: Wave and Turing instabilities of wavenumber k for different α and given $\mu = \frac{1}{2}$. The separating wave numbers k_{A}, k_{B} and k_{c} are drawn as black, gray, and dashed line, respectively. For $\alpha > \tilde{\alpha}$, the critical k of the wave instability is given by k_{W}, drawn as dotted line.

and illustrated in Fig. 10. For $\alpha > (1-\mu^2)/(2\,(1+\mu^2))$, k_{A} and k_{B} cease and waves are possible for all k with $0 < k < k_{\mathrm{c}}$.

For a wave instability, the real part of $\lambda(k)$ is given by $(f_1(k) + f_2(k))/2$. Its maximum is located at $k_{\mathrm{W}}^2 = (1+\mu^2)/(1+\mu^4)$ and with $\mathrm{Re}[\lambda(k_{\mathrm{W}})] = 0$, we find the critical value

$$\eta_{\mathrm{W}} = \frac{(1-\mu^2)^2}{2\,(1+\mu^4)}\,, \tag{25}$$

which is shown for $\mu = 1/2$ as (solid and dashed) vertical red line in Fig. 1. This line only exists for values of α which ensure that the root term of $\lambda(k_{\mathrm{W}})$ is imaginary, see Fig. 10, a condition which can be expressed as

$$\alpha > \tilde{\alpha} = \frac{(1-\mu^2)^2\,(1-\mu^4)}{2\,(1+\mu^4)^2}. \tag{26}$$

For $\alpha < \tilde{\alpha}$, the real part of λ takes its maximal value for $k = k_{\mathsf{B}}$. With $\lambda(k_{\mathsf{B}}) = 0$, we find

$$\eta_{\mathrm{W}}(\alpha) = \frac{1+\mu^4 - 2\mu^2\sqrt{1 - 2\,\alpha\,\frac{1+\mu^2}{1-\mu^2}}}{(1+\mu^2)^2} - \frac{1+\mu^4}{1-\mu^4}\,\alpha\,, \tag{27}$$

which is displayed as bent and dashed red line in Fig. 1.

In case of a Turing instability, the root term in Eq. (21) is real. Without loss of generality, we set $\lambda_1(k) = 0$ and $\partial_k\lambda_1(k) = 0$ at the instability line, resulting in

$$\begin{aligned} 0 &= \lambda_1(k)\,\partial_k\lambda_2(k) + \partial_k\lambda_1(k)\,\lambda_2(k) = \partial_k\,(\lambda_1(k)\,\lambda_2(k)) \\ &= \partial_k \det L(k) = \partial_k\,(f_1(k) f_2(k))\,. \end{aligned} \tag{28}$$

Taking advantage of the symmetry of the system, we introduce $K = k^2$ and $F_i(K) = f_i(k)$ to obtain a cubic equation in K:

$$\partial_K\,(F_1(K)F_2(K)) = 0\,, \tag{29}$$

for which analytic solutions $K_1(\eta), K_2(\eta)$ and $K_3(\eta)$ exist for given η. The relation $K_1(\eta) > 1/\mu^2$ corresponds to the Turing instability of small wavelength emerging out of Eq. (1b). The bifurcation line of this instability (black solid and dashed line in Fig. 1) is computed by setting $F_1(K_1)\,F_2(K_1) + \alpha_{\mathrm{T}}^2 = 0$ and solving for $\alpha_{\mathrm{T}}(\eta) > 0$:

$$\alpha_{\mathrm{T}}(\eta) = \sqrt{-F_1(K_1(\eta))\,F_2(K_1(\eta))}\,. \tag{30}$$

The solution $K_2(\eta) < 1$ corresponds to the Turing instability of larger wavelength emerging from Eq. (1a). Its bifurcation line is computed in an analogous manner and displayed as black dotted line in Fig. 1. Finally, the third solution $K_3(\eta)$ does yield positive values of $F_1(K_3)\,F_2(K_3)$ for $\eta > 0$ and thus does not provide another instability.

At the codimension-two point, the maxima of $\lambda(k)$ related to the small wavelength Turing instability and the wave instability cross the real axis simultaneously, i.e. the corresponding bifurcation lines intersect. In parameter space, this point is

$$\eta_\mathrm{c} = \eta_\mathrm{W} = \frac{(1-\mu^2)^2}{2\,(1+\mu^4)}\,, \tag{31}$$

$$\begin{aligned}\alpha_\mathrm{c} &= \alpha_\mathrm{T}(\eta_\mathrm{c}) \\ &= \sqrt{-\left(\eta_\mathrm{c} - (1-K_1(\eta_\mathrm{c}))^2\right)\left(\eta_\mathrm{c} - (1-\mu^2 K_1(\eta_\mathrm{c}))^2\right)}.\end{aligned} \tag{32}$$

and the critical wave numbers for the wave and Turing instability are given by

$$k_\mathrm{W}^2 = \frac{1+\mu^2}{1+\mu^4} \tag{33}$$

and

$$k_\mathrm{T}^2 = K_1(\eta_\mathrm{c}) \tag{34}$$

respectively. The angular frequency ω of the wave is given by

$$\omega^2 = \left(\mathrm{Im}\left[\lambda(k_\mathrm{W})\right]\right)^2 = \alpha_\mathrm{c}^2 - \frac{(1-\mu^2)^4(1-\mu^4)^2}{4(1+\mu^4)^4}\,. \tag{35}$$

B Derivation of the amplitude equations

For a formal derviation of the amplitude equations we adapt the scheme provided in [10]. Recall the ansatz in Eq. (3) which reads

$$\boldsymbol{u}(t,x) = \varepsilon \boldsymbol{u}_1 + \varepsilon^2 \boldsymbol{u}_2 + \varepsilon^3 \boldsymbol{u}_3 + \mathcal{O}(\varepsilon^4), \tag{36}$$

wherein each summand in the expansion is of the form

$$\begin{aligned}\boldsymbol{u}_n(t,x) = \big[&A_\mathrm{L}^n(\varepsilon t, \varepsilon^2 t, \varepsilon x, \varepsilon^2 x) e^{i(k_\mathrm{W} x + \omega t)} \boldsymbol{u}_\mathrm{L} \\ &+ A_\mathrm{R}^n(\varepsilon t, \varepsilon^2 t, \varepsilon x, \varepsilon^2 x) e^{i(k_\mathrm{W} x - \omega t)} \boldsymbol{u}_\mathrm{R} \\ &+ A_\mathrm{T}^n(\varepsilon t, \varepsilon^2 t, \varepsilon x, \varepsilon^2 x) e^{i(k_\mathrm{T} x)} \boldsymbol{u}_\mathrm{T} + \mathrm{c.c.}\big]\end{aligned} \tag{37}$$

with $\boldsymbol{u}_k$ denoting the eigenvectors for $k \in \{\mathrm{L}, \mathrm{R}, \mathrm{T}\}$ of the eigenvalue problems in (40) below. We can reformulate the SHEs in terms of

$$\partial_t \boldsymbol{u} = \mathcal{L}(\boldsymbol{u}) + \mathcal{N}(\boldsymbol{u})\,, \tag{38}$$

where $\mathcal{L}$ denotes the linear part and $\mathcal{N}$ the nonlinear, cubic part. If one introduces the slow scales as in Sec. 3.1, the derivatives transform via

$$\partial_t \to \partial_t + \varepsilon \partial_{\tau_1} + \varepsilon_{\tau_2}^2 \qquad \partial_x \to \partial_x + \varepsilon \partial_{\chi_1} + \varepsilon^2 \partial_{\chi_2}\,. \tag{39}$$

Inserting Eqs. (36)–(37) into Eq. (38) or rather Eq. (1) and expanding in orders of ε gives the following: on the order ε^1 we recover the eigenvalue problems for the critical modes

$$i\omega \boldsymbol{u}_{\mathrm{L/R}} = \pm L(k_{\mathrm{W}})\boldsymbol{u}_{\mathrm{L/R}}, \quad 0 = L(k_{\mathrm{T}})\boldsymbol{u}_{\mathrm{T}}\,, \tag{40}$$

where the matrix L is given in Eq. (20). On the order of ε^2 we find for $c = \mathrm{Im}[\lambda'(k_{\mathrm{W}})]$

$$(\partial_{\tau_1} \mp c\partial_{\chi_1})A^1_{\mathrm{L/R}} = 0, \quad \partial_{\tau_1} A^1_{\mathrm{T}} = 0\,, \tag{41}$$

while assuming $L'(k_W)\boldsymbol{u}_{\mathrm{L/R}} = \pm\lambda'(k_{\mathrm{W}})\boldsymbol{u}_{\mathrm{L/R}}$, cf. Appendix A in [10]. For the group velocity c one finds the expression

$$c = \frac{2\mu^2\left(1-\mu^2\right)^4\left(1+\mu^2\right)^{\frac{3}{2}}}{\left(1+\mu^4\right)^{\frac{7}{2}}\sqrt{\alpha_{\mathrm{c}}^2 - \frac{(1-\mu^2)^6(1+\mu^2)^2}{4(1+\mu^4)^4}}}\,. \tag{42}$$

Note that $\mathrm{Re}[\lambda'(k_{\mathrm{W}})] = 0$ and that the solvability condition for A_{T} simply yields $A_{\mathrm{T}} = A_{\mathrm{T}}(\tau_2, \chi_1, \chi_2)$. The relevant equations on the order of ε^3 are

$$\begin{aligned}
&(\partial_{\tau_2} - c\partial_{\chi_2})A^1_{\mathrm{L}} + (\partial_{\tau_1} - c\partial_{\chi_1})A^2_{\mathrm{L}} \\
&= \kappa_{\mathrm{W}}A^1_{\mathrm{L}} + D_{\mathrm{W}}\partial_{\chi_1\chi_1}A^1_{\mathrm{L}} + \sigma_{\mathrm{W}}|A^1_{\mathrm{L}}|^2A^1_{\mathrm{L}} \\
&\quad + \sigma_{\mathrm{WW}}|A^1_{\mathrm{R}}|^2A^1_{\mathrm{L}} + \sigma_{\mathrm{WT}}|A^1_{\mathrm{T}}|^2A^1_{\mathrm{L}}\,, \\
&(\partial_{\tau_2} - c\partial_{\chi_2})A^1_{\mathrm{R}} + (\partial_{\tau_1} - c\partial_{\chi_1})A^2_{\mathrm{R}} \\
&= \overline{\kappa}_{\mathrm{W}}A^1_{\mathrm{R}} + \overline{D}_{\mathrm{W}}\partial_{\chi_1\chi_1}A^1_{\mathrm{R}} + \sigma_{\mathrm{W}}|A^1_{\mathrm{R}}|^2A^1_{\mathrm{R}} \\
&\quad + \sigma_{\mathrm{WW}}|A^1_{\mathrm{L}}|^2A^1_{\mathrm{R}} + \overline{\sigma}_{\mathrm{WT}}|A^1_{\mathrm{T}}|^2A^1_{\mathrm{R}}\,, \\
&\partial_{\tau_2}A^1_{\mathrm{T}} + \partial_{\tau_1}A^2_{\mathrm{T}} \\
&= \kappa_{\mathrm{T}}A^1_{\mathrm{T}} + D_{\mathrm{T}}\partial_{\chi_1\chi_1}A^1_{\mathrm{T}} + \sigma_{\mathrm{T}}|A^1_{\mathrm{T}}|^2A^1_{\mathrm{T}} \\
&\quad + \sigma_{\mathrm{TW}}(|A^1_{\mathrm{L}}|^2 + |A^1_{\mathrm{R}}|^2)A^1_{\mathrm{T}}\,.
\end{aligned} \tag{43}$$

By arguing that the amplitudes in the expansion in (36)–(37) must not contain any secular conditions, i.e. terms that grow linearly in time, we obtain $(\partial_{\tau_1} - c\partial_{\chi_1})A^2_{\mathrm{L/R}} = 0$, cf. Appendix B in [10], and, therefore, system (4)–(5) follows immediately.

Moreover, let $D_{\mathrm{W}} = -\frac{1}{2}\lambda''(k_{\mathrm{W}})$ and $D_{\mathrm{T}} = -\frac{1}{2}\lambda''(k_{\mathrm{T}})$. For the wave diffusion constant D_{W} the real part has a simple analytic expression

$$D_{\mathrm{W}} = 2(1+\mu^2) + i\,\mathrm{Im}[D_{\mathrm{W}}]\,. \tag{44}$$

The imaginary part of D_{W} as well as D_{T} can also be expressed analytically but in an intricate and

uninstructive way. The remaining coefficients are

$$\kappa_{\mathrm{W}} = \frac{\boldsymbol{v}_{\mathrm{L}} \cdot M\boldsymbol{u}_{\mathrm{L}}}{\boldsymbol{v}_{\mathrm{L}} \cdot \boldsymbol{u}_{\mathrm{L}}} = \eta_{\mathrm{p}} - i\frac{\alpha_{\mathrm{c}}\alpha_{\mathrm{p}}}{\omega}\,, \tag{45}$$

$$\kappa_{\mathrm{T}} = \frac{\boldsymbol{v}_{\mathrm{T}} \cdot M\boldsymbol{u}_{\mathrm{T}}}{\boldsymbol{v}_{\mathrm{T}} \cdot \boldsymbol{u}_{\mathrm{T}}} = \eta_{\mathrm{p}} + \frac{2\alpha_{\mathrm{c}}\alpha_{\mathrm{p}}a_{\mathrm{T}}}{a_{\mathrm{T}}^2 - \alpha_{\mathrm{c}}^2}\,, \tag{46}$$

$$\sigma_{\mathrm{W}} = -\frac{3}{4}\frac{\boldsymbol{v}_{\mathrm{L}} \cdot A(\boldsymbol{u}_{\mathrm{L}})\boldsymbol{u}_{\mathrm{L}}}{\boldsymbol{v}_{\mathrm{L}} \cdot \boldsymbol{u}_{\mathrm{L}}} = -\frac{3}{4}\alpha_{\mathrm{c}}^2\,, \tag{47}$$

$$\sigma_{\mathrm{T}} = -\frac{3}{4}\frac{\boldsymbol{v}_{\mathrm{T}} \cdot A(\boldsymbol{u}_{\mathrm{T}})\boldsymbol{u}_{\mathrm{T}}}{\boldsymbol{v}_{\mathrm{T}} \cdot \boldsymbol{u}_{\mathrm{T}}} = -\frac{3}{4}(a_{\mathrm{T}}^2 + \alpha_{\mathrm{c}}^2)\,, \tag{48}$$

$$\sigma_{\mathrm{WW}} = -\frac{3}{2}\frac{\boldsymbol{v}_{\mathrm{L}} \cdot A(\boldsymbol{u}_{\mathrm{R}})\boldsymbol{u}_{\mathrm{L}}}{\boldsymbol{v}_{\mathrm{L}} \cdot \boldsymbol{u}_{\mathrm{L}}} = -\frac{3}{2}\alpha_{\mathrm{c}}^2\,, \tag{49}$$

$$\sigma_{\mathrm{WT}} = -\frac{3}{2}\frac{\boldsymbol{v}_{\mathrm{L}} \cdot A(\boldsymbol{u}_{\mathrm{T}})\boldsymbol{u}_{\mathrm{L}}}{\boldsymbol{v}_{\mathrm{L}} \cdot \boldsymbol{u}_{\mathrm{L}}} \tag{50}$$

$$= -\frac{3}{4}\left(a_{\mathrm{T}}^2 + \alpha_{\mathrm{c}}^2 + i\frac{a_{\mathrm{W}}}{\omega}(\alpha_{\mathrm{c}}^2 - a_{\mathrm{T}}^2)\right)\,, \tag{51}$$

$$\sigma_{\mathrm{TW}} = -\frac{3}{2}\frac{\boldsymbol{v}_{\mathrm{T}} \cdot A(\boldsymbol{u}_{\mathrm{L}})\boldsymbol{u}_{\mathrm{T}}}{\boldsymbol{v}_{\mathrm{T}} \cdot \boldsymbol{u}_{\mathrm{T}}} = -\frac{3}{2}\alpha_{\mathrm{c}}^2\,. \tag{52}$$

For brevity, we introduced $a_{\mathrm{W}} = f_1(k_{\mathrm{W}})$ and $a_{\mathrm{T}} = f_1(k_{\mathrm{T}})$, as well as the matrix $A(v) = \mathrm{diag}\,(|v_1|^2, |v_2|^2)$.

References

[1] S. Alonso, K. John, and M. Bär. Complex wave patterns in an effective reaction–diffusion model for chemical reactions in microemulsions. *J. Chem. Phys.*, 134(9):094117, 2011.

[2] I. Berenstein and J. Carballido-Landeira. Spatiotemporal chaos involving wave instability. *Chaos*, 27(1):013116, 2017.

[3] C. Beta and K. Kruse. Intracellular oscillations and waves. *Annu. Rev. Condens. Matter Phys.*, 8:239–264, 2017.

[4] M. Cross and H. Greenside. *Pattern formation and dynamics in nonequilibrium systems*. Cambridge University Press, 2009.

[5] M. C. Cross and P. C. Hohenberg. Pattern formation outside of equilibrium. *Rev. Mod. Phys.*, 65(3):851–1112, 1993.

[6] A. De Wit, D. Lima, G. Dewel, and P. Borckmans. Spatiotemporal dynamics near a codimension-two point. *Phys. Rev. E*, 54:261–271, Jul 1996.

[7] N. Dirr and N. K. Yip. Pinning and de-pinning phenomena in front propagation in heterogeneous media. *Interfaces and Free Boundaries*, 8(1):79–109, 2006.

[8] P. Gross, K. V. Kumar, and S. W. Grill. How active mechanics and regulatory biochemistry combine to form patterns in development. *Annu. Rev. Biophys.*, 46(1):337, 2017.

[9] S. V. Gurevich and R. Friedrich. Instabilities of localized structures in dissipative systems with delayed feedback. *Phys. Rev. Lett.*, 110:014101, Jan 2013.

[10] W. Just, F. Matthäus, H. R. Völger, C. Just, B. Rumpf, and A. Riegert. Weakly nonlinear analysis in spatially extended systems as a formal perturbation scheme. *arXiv preprint*, 1997.

[11] R. Kapral and K. Showalter. *Chemical waves and patterns*, volume 10. Springer Science & Business Media, 2012.

[12] S. Kinast, Y. R. Zelnik, G. Bel, and E. Meron. Interplay between turing mechanisms can increase pattern diversity. *Phys. Rev. Lett.*, 112(7):078701, 2014.

[13] P. Kirrmann, G. Schneider, and A. Mielke. The validity of modulation equations for extended systems with cubic nonlinearities. *Proc. Roy. Soc. Edinburgh Sect. A*, 122(1-2):85–91, 1992. ISSN 0308-2105. URL https://doi.org/10.1017/S0308210500020989.

[14] E. Knobloch. Remarks on the use and misuse of the ginzburg-landau equation. *Pitman research notes in mathematics series*, pages 130–130, 1995.

[15] S. Kondo and T. Miura. Reaction-diffusion model as a framework for understanding biological pattern formation. *Science*, 329(5999):1616–1620, 2010.

[16] A. Kulka, M. Bode, and H.-G. Purwins. On the influence of inhomogeneities in a reaction-diffusion system. *Phys. Lett. A*, 203(1):33 – 39, 1995.

[17] J. Lega, J. V. Moloney, and A. C. Newell. Swift-Hohenberg equation for lasers. *Phys. Rev. Lett.*, 73:2978–2981, Nov 1994.

[18] J. Löber and H. Engel. Controlling the position of traveling waves in reaction-diffusion systems. *Phys. Rev. Lett.*, 112 (14):148305, 2014.

[19] M. Meixner, A. De Wit, S. Bose, and E. Schöll. Generic spatiotemporal dynamics near codimension-two turing-hopf bifurcations. *Phys. Rev. E*, 55:6690–6697, Jun 1997.

[20] E. Meron. *Nonlinear physics of ecosystems*. CRC Press, 2015.

[21] A. Mielke. The Ginzburg-Landau equation in its role as a modulation equation. In *Handbook of dynamical systems, Vol. 2*, pages 759–834. North-Holland, Amsterdam, 2002.

[22] A. Mielke. Deriving amplitude equations via evolutionary Γ-convergence. *Discrete Contin. Dyn. Syst.*, 35(6):2679–2700, 2015. ISSN 1078-0947.

[23] D. Miguez, E. Nicola, A. Munuzuri, J. Casademunt, F. Sagués, and L. Kramer. Traveling-stripe forcing generates hexagonal patterns. *Phys. Rev. Lett.*, 93(4):048303, 2004.

[24] A. C. Newell and J. A. Whitehead. Finite bandwidth, finite amplitude convection. *Journal of Fluid Mechanics*, 38(2): 279–303, 1969.

[25] E. M. Nicola, M. Or-Guil, W. Wolf, and M. Bär. Drifting pattern domains in a reaction-diffusion system with nonlocal coupling. *Phys. Rev. E*, 65(5):055101, 2002.

[26] C. Punckt, M. Stich, C. Beta, and H. H. Rotermund. Suppression of spatiotemporal chaos in the oscillatory co oxidation on pt (110) by focused laser light. *Phys. Rev. E*, 77(4):046222, 2008.

[27] L. Rapp, F. Bergmann, and W. Zimmermann. Pattern orientation in finite domains without boundaries. *EPL*, 113(2): 28006, 2016.

[28] I. Rehberg and G. Ahlers. Experimental observation of a codimension-two bifurcation in a binary fluid mixture. *Phys. Rev. Lett.*, 55(5):500, 1985.

[29] F. Sagués, D. G. Míguez, E. M. Nicola, A. P. Muñuzuri, J. Casademunt, and L. Kramer. Travelling-stripe forcing of turing patterns. *Physica D*, 199(1):235–242, 2004.

[30] T. Sakurai, E. Mihaliuk, F. Chirila, and K. Showalter. Design and control of wave propagation patterns in excitable media. *Science*, 296(5575):2009–2012, 2002.

[31] Y. Sasai. Cytosystems dynamics in self-organization of tissue architecture. *Nature*, 493(7432):318, 2013.

[32] G. Schneider. Validity and limitation of the Newell–Whitehead equation. *Math. Nachr.*, 176:249–263, 1995. ISSN 0308-2105.

[33] D. Schüler, S. Alonso, A. Torcini, and M. Bär. Spatio-temporal dynamics induced by competing instabilities in two asymmetrically coupled nonlinear evolution equations. *Chaos*, 24(4):043142, 2014.

[34] N. Stoop, R. Lagrange, D. Terwagne, P. M. Reis, and J. Dunkel. Curvature-induced symmetry breaking determines elastic surface patterns. *Nat. Mater.*, 14(3):337–342, 2015.

[35] H. L. Swinney and J. P. Gollub. *Hydrodynamic instabilities and the transition to turbulence*. Springer, 1985.

[36] C. E. Tarnita, J. A. Bonachela, E. Sheffer, J. A. Guyton, T. C. Coverdale, R. A. Long, and R. M. Pringle. A theoretical foundation for multi-scale regular vegetation patterns. *Nature*, 541(7637):398–401, 2017.

[37] M. van Hecke, C. Storm, and W. van Saarloos. Sources, sinks and wavenumber selection in coupled CGL equations and experimental implications for counter-propagating wave systems. *Physica D*, 134(February 2008):1–47, 1999.

[38] P. van Heijster, A. Doelman, T. J. Kaper, Y. Nishiura, and K.-I. Ueda. Pinned fronts in heterogeneous media of jump type. *Nonlinearity*, 24(1):127, 2011.

[39] V. K. Vanag and I. R. Epstein. Pattern Formation in a Tunable Medium: The Belousov-Zhabotinsky Reaction in an Aerosol OT Microemulsion. *Phys. Rev. Lett.*, 87(22):228301, 2001.

[40] L. Yang, M. Dolnik, A. M. Zhabotinsky, and I. R. Epstein. Pattern formation arising from interactions between turing and wave instabilities. *J. Chem. Phys.*, 117(15):7259–7265, 2002.